

Mass sensitivity of gravimetric satellites

Robert Spero
25 August 2020

Jet Propulsion Laboratory, California Institute of Technology, Pasadena, California 91109, USA

arXiv:2006.08179v3 [physics.geo-ph] 26 Aug 2020

Corresponding author: Robert Spero, spero@jpl.nasa.gov

Abstract

A point mass on the surface of the Earth gives the highest frequency content for orbiting gravimetric measurements, with the maximum frequency for gradiometers or satellite-to-satellite tracking determined by orbital altitude. Frequency-domain expressions are found for orbiting gravimetric measurements of a point-like source on the surface of the Earth. The response of orbiting gradiometers such as GOCE and satellite-to-satellite tracking missions such as GRACE-FO are compared. The optimal signal-to-noise ratio as a function noise of the measurement apparatus is computed, and from that the minimum detectable mass is inferred. The point mass magnitude that gives signal-to-noise ratio = 3 is for GOCE $M_3 = 200$ Gton and for the laser ranging interferometer measurement on GRACE-FO $M_3 = 0.5$ Gton. For the laser ranging interferometer measurement, the optimal filter for detecting point-like masses has a passband of 1 to 20 mHz, differing from the 0.3 to 20 mHz admittance filter of Ghobadi-Far et al. (2018), which is not specialized for detecting point-like masses. M_3 for future GRACE-like missions with different orbital parameters and improved instrument sensitivity is explored, and the optimum spacecraft separation is found to be approximately a factor of 1.7 larger than the orbital altitude.

Plain Language Summary

The twin-satellite mission GRACE-FO has been measuring Earth’s changing gravity for two years, as did its predecessor GRACE for 15 years. These missions have provided information on large-scale motion of water and ice melting, information that was previously unavailable. In the next ten years more such mass-change measuring satellites will be launched to continue the gravity record with improved precision. Yet there has been no single-number answer to the question, how precisely is gravity measured by such missions? This paper derives a prescription for a sensitivity figure of merit, namely mass resolution. GRACE-FO is found to be capable in principle of measuring masses as small as 500 Mton. To set the scale, melting of Greenland ice at the rate of 300 Gton/year is easily measured by GRACE, while the weight of all the buildings in a large city is only 100 Mton. Future missions may have sensitivity on the order of 10 Mton. The mass resolution formulation developed in this paper allows an optimization of orbit and payload instruments for more precise measurements of known sources such as glaciers and changing sea level, and to discover new sources such as underground water storage that are too small to be observed by existing satellites. To achieve the best sensitivity, the data generated by the instruments on the spacecraft are processed by a filter that is tailored to the measurement noise.

1 Introduction

A global gravity map is the principal data product of satellite gravity missions. Previously CHAMP (Reigber et al., 2003), GRACE (Tapley et al., 2004), and GOCE (Drinkwater et al., 2006) collected data to map the Earth’s gravity, and GRAIL Konopliv et al. (2013) measured the Moon’s gravity. Currently GRACE Follow-On (GRACE-FO) (Landerer et al., 2020) is extending the GRACE data record, with increased ranging precision afforded by its laser ranging interferometer (LRI) (Abich et al., 2019).

As observed by Watkins et al. (2015), the most commonly used method to analyze satellite gravity data is based on global gravity fields expressed in terms of spherical harmonic basis functions. An alternative to spherical harmonics is the mass concentration, or mascon, solution. Starting with Wong et al. (1971), the mascon approach was applied to single-satellite lunar orbital measurements to infer the surface gravity of the moon. Mascons may be modeled as many spherical caps (Pollack (1973), Watkins

et al. (2005)) that cover the globe, or used to solve for regional fields. An example of mascons applied to regional fields of the Moon is Han (2013).

Though they differ in methods and slightly in results, the spherical harmonic and mascon methods are constructed to answer the same question: what is the gravity field that is most consistent with measurements? Here we address a different question. What is the limit to measurement precision of a specified feature, namely a point-like mass on the surface? This is an artificial model, a single mascon, that is not directly applicable to the geodesy agenda of measuring the Earth's gravity. The motivation for this analysis is twofold: to provide a single-number figure of merit, namely the minimum detectable mass perturbation, and to find the optimal filter for such a detection. The minimum detectable mass M_3 is defined as the point mass that gives signal-to-noise ratio $\rho = 3$ in a single orbital pass. It is calculated by the formalism of Wiener optimal filter applied to the problem of detecting a signal of known form, against a background specified by instrument power spectral density (Wainstein & Zubakov, 1970). A comparison of M_3 for different orbital configurations and instrument sensitivities guides the design of future missions. Additionally, we find the optimum satellite separation in GRACE-like missions for a specified instrument noise power spectral density.

2 Gradiometer Mass Sensitivity

Consider a gradiometer flying directly over a point mass M at altitude h , Figure 1 left. At orbital altitude $h = 330$ km, the along-track velocity v is the orbital velocity

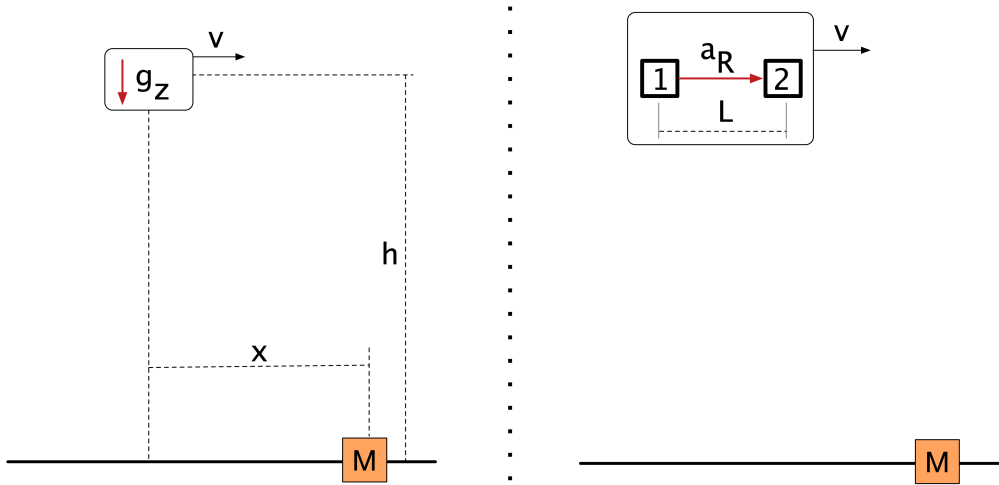


Figure 1. Measurement of gravitational field from a point mass M at along-track distance x , altitude h , and velocity v . *Left:* Vertical gradient g_z . *Right:* Differential acceleration a_R between spacecraft 1 and 2 with average separation L .

$v_o = 7.7$ km/s and the along-track distance x changes at approximately constant rate, $x = v_o t$. The gradient in the vertical, z direction as a function of time is

$$g_z(t) = \frac{GM}{(h^2 + (v_o t)^2)^{3/2}} = \kappa_g (1 + (f_h t)^2)^{-3/2} \quad (1)$$

where G is Newton's constant of gravitation, $f_h = v_o/h$, and $\kappa_g = GM/h^3 = 1.85 \times 10^{-3}$ mE for $(h, M) = (330 \text{ km}, 1 \text{ Gton})$; $1 \text{ mE} = 1 \times 10^{-12} \text{ s}^{-2}$.

Taking the fourier transform,

$$\mathcal{F}[g_z(t)] = g_z(f) = \kappa_g \frac{4\pi f}{f_h^2} \cdot K_1\left(\frac{2\pi f}{f_h}\right) \quad (2)$$

where K_1 is the modified bessel function of the 2nd kind, order 1. The fourier transform $g_z(f)$ has signal energy down to zero frequency and roll-off frequency $f_h = 30$ mHz.

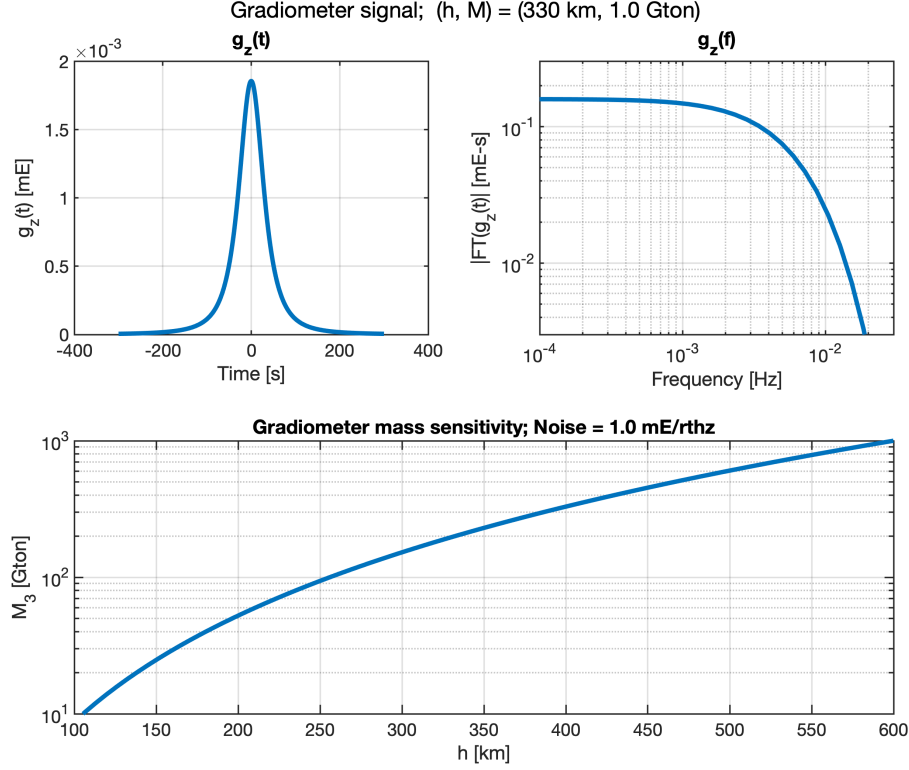


Figure 2. Orbiting gradiometer vertical gradient response to a point mass. Upper left: time domain; Upper right: Fourier transform of time domain; Lower: Detectable mass with signal-to-noise = 3.

The signal-to-noise ratio depends on the power spectral density of the gradiometer noise, $S_g(f)$. Define the frequency-dependent signal-to-noise density

$$W_{g_z}(f) = \frac{|g_z(f)|^2}{S_g(f)}. \quad (3)$$

Let the signal per unit source mass $g'_z(f) = g_z(f)/M$ and $W'_{g_z}(f) = W_{g_z}(f)/M$. Following Flanagan and Hughes (1998), the maximum signal-to-noise ratio per unit source mass ρ' is given by Wiener optimal filter theory as

$$\rho' = \sqrt{4 \int_0^\infty W'_{g_z}(f) df}. \quad (4)$$

It follows that the minimum detectable mass with $\rho = 3$ is

$$M_3 = \frac{3}{\sqrt{4 \int_0^\infty W'_{g_z}(f) df}}. \quad (5)$$

The lower panel of Figure 2 shows M_3 as a function of orbital altitude h for a gradiometer limited by white spectral noise $S_g(f) = 1 \text{ mE}/\sqrt{\text{Hz}}$, the assumed noise in the GOCE gradiometer. At $h = 330 \text{ km}$, $M_3 = 200 \text{ Gton}$. The corresponding peak gradient observed is $\kappa_g(M_3) = 0.37 \text{ mE}$.

3 Sensitivity of GRACE-like measurements

The measurement configuration and signal parameters for the low-low satellite-to-satellite tracking (SST) of GRACE and GRACE-FO are shown in Figure 1, right. The primary signal is the along-track differential position of the spacecraft, measured by microwave ranging or laser interferometry.

3.1 Single Spacecraft Acceleration

Neglecting orbital dynamics, which influence the measurement mostly at low frequency compared to the high-frequency point-mass perturbation under consideration, the acceleration on spacecraft 1 flying over point mass M at along-track distance x is $a_1 = -GMx/(h^2 + x^2)^{3/2}$.

Define the acceleration per unit source mass, $a'_1 = a_1/M$. Then

$$a'_1 = -\frac{Gtv_o}{(h^2 + t^2v_o^2)^{3/2}} \quad (6)$$

Converting to frequency space,

$$a'_1(f) = \mathcal{F}[a'_1(t)] = \frac{4\pi i f G K_0 \left(\frac{2\pi f}{f_h}\right)}{v_o^2}, \quad (7)$$

where K_0 is the modified bessel function of the 2nd kind, order 0.

3.2 Range Acceleration Signal

The acceleration experienced by spacecraft 2 is the same as spacecraft 1 at distance L , but delayed by $\tau = L/v_o$. The resulting (along-track) range acceleration between the spacecraft (Figure 3, left) is similar to what Han (2013) computed for the the response of GRAIL spacecraft to regional lunar gravity. The peak range acceleration a_R^p is

$$a_R^p = \frac{GL}{(h^2 + (L/2)^2)^{3/2}} M \equiv \kappa_R(L, h)M. \quad (8)$$

Using the identity $\mathcal{F}(\text{delay } \tau) = \exp(-2\pi i f \tau)$, the range acceleration in the frequency domain, $a_R(f)$, is given by

$$a'_R(f) = a'_1(f)(1 - e^{-2\pi i f \tau}) \quad (9)$$

$$|a'_R(f)| = 2|a'_1(f)| \sin(\pi f \tau) \quad (10)$$

$$(11)$$

That is, in the frequency domain the range acceleration is the single-satellite acceleration multiplied by $2|\sin(\pi f \tau)|$. For $f \ll 1/\tau$, $|a_R(f)| \propto L$, which is the response for the spacecraft pair acting as a gradiometer. The response departs from that of a gradiometer at large L , most conspicuously in the form of high-frequency nulls. The first null is at $f_{\text{null}} = 1/\tau = 38 \text{ mHz}$ for low-earth orbit and $L = 200 \text{ km}$, as recognized by Wolff (1969). In degree-variance evaluations of measurement sensitivity, the first null is expressed as a maximum in geoid height error at degree $N = f_{\text{null}}/f_1 = 216$ for $L = 200 \text{ km}$, and $N = 86$ for $L = 500 \text{ km}$, where $f_1 = \text{orbital frequency} = 0.176 \text{ mHz}$.

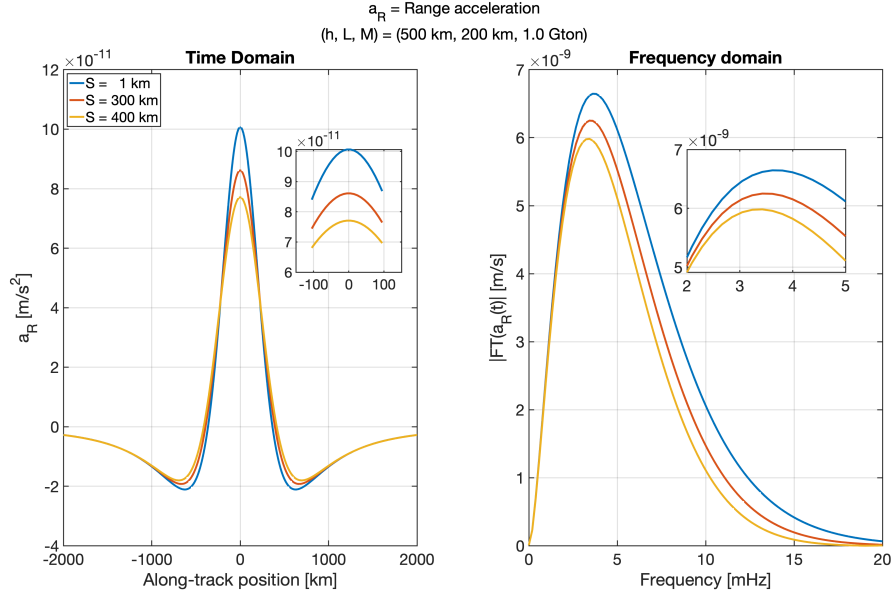


Figure 3. Range acceleration resulting from a square mass centered under the flight along-track path. Orbital altitude h , average spacecraft separation L and source mass M are indicated in the title. The separate traces are for squares of side S indicated in the legend. *Left:* time domain; *Right:* frequency domain = Fourier Transform of time-domain.

From Equations 7 and 10,

$$|a'_R(f)| = \frac{8\pi f G}{v_o^2} \left| K_0 \left(\frac{2\pi f}{f_h} \right) \right| \left| \sin \left(\frac{2\pi f}{f_L} \right) \right|, \quad (12)$$

where

$$\begin{aligned} v_o &= \text{orbital velocity} && = 7.6 \text{ km/s} \\ h &= \text{orbital altitude} && = 500 \text{ km} \\ L &= \text{spacecraft separation} && = 200 \text{ km} \\ f_h &= \frac{v_o}{h} && = 15.5 \text{ mHz} \\ f_L &= \frac{v_o}{L/2} && = 76 \text{ mHz} \\ \tau &= \frac{L}{v_o} && = 26 \text{ s} \\ \kappa_R(L, h) &= \frac{GL}{(h^2 + (L/2)^2)^{3/2}} && = 0.101 \text{ nm/s}^2/\text{Gton}. \end{aligned}$$

Numerical values apply to GRACE-FO.

From Abramowitz and Stegun (1964), 9.7.2, $K_0(z) \sim \sqrt{\pi/(2z)}e^{-z}$, where \sim indicates approximately equal for large z . It follows that $2f K_0(2\pi f/f_h) \sim \sqrt{f f_h} \exp(-2\pi f/f_h)$, and the high-frequency limit of Equation 12 is

$$|a'_R(f)| = \frac{4\pi G}{v_o^2} \sqrt{f f_h} e^{-2\pi f/f_h} \left| \sin \left(\frac{2\pi f}{f_L} \right) \right|. \quad (13)$$

At high frequency the measurement response is attenuated approximately exponentially with characteristic frequency $f_h/(2\pi) = 2.5 \text{ mHz}$. This corresponds to harmonic

order $f_h/(2\pi f_1) \approx 14$, where $f_1 = 0.176$ mHz is the orbital frequency. In general, realistic mass distributions will result in more attenuation at high frequency than a point mass.

To explore the valid realm of the point-mass approximation, Figure 3 shows the range acceleration signal from a square-shaped mass of side length S , computed by numerical integration. The $S=1$ km result is in agreement with the point-mass analytical calculation, which is valid at the 20% level for sources as large as $S=300$ km. Henceforth, we restrict analysis to the signal from a point source.

As shown in Pollack (1973), Figure 3, the degree power spectrum for a point mass is the same for all harmonic degrees: a white spectrum. Equation 12 gives the measurement impulse response; that is, the range acceleration frequency response to a point mass input. This facilitates the direct comparison of signal and noise amplitudes as computed in the following section, and yields an expression for the minimum detectable mass for GRACE-like measurements of point-like perturbations to surface gravity.

3.3 Noise and Mass Sensitivity

Consider the range measurement made by the laser ranging interferometer (LRI) on GRACE-FO. Assuming the measurement resolution is limited by thermal noise of the laser reference cavity (Numata et al., 2004), the displacement noise root power spectral density (rpsd) \tilde{x}_{LRI} and strain rpsd \tilde{x}_{LRI}/L are given by

$$\tilde{x}_{\text{LRI}}(f)/L = x_c/\sqrt{f}, \quad (14)$$

where x_c is a constant. For the LRI (Abich et al., 2019), $x_c = 1 \times 10^{-15}$. The rpsd of the LRI range acceleration noise is

$$\sqrt{S_{\text{LRI}}(f)} = (2\pi f)^2 \cdot \tilde{x}_{\text{LRI}}(f). \quad (15)$$

Take for the accelerometer measurement noise rpsd on GRACE and GRACE-FO (Touboul et al., 1999)

$$\sqrt{S_{\text{ACC}}(f)} = \tilde{a}_0 \sqrt{1 + \left(\frac{f_k}{f}\right)^2}, \quad (16)$$

with $\tilde{a}_0 =$ acceleration white noise $= 1 \times 10^{-10}$ m/s²/√Hz, $f_k = 5$ mHz. Improved accelerometers in future missions (Christophe et al., 2010), (Conklin & Nguyen, 2017) may have $\tilde{a}_0 = 1 \times 10^{-12}$ m/s²/√Hz or better. Assuming that the accelerometers have uncorrelated noise, the total S_{ACC} is the sum of the S_{ACC} from each spacecraft. We assume that the non-inertial acceleration noise is equal to the accelerometer sensing noise. This is a conservative assumption in that for part of the spectrum modeled disturbances for solar radiation pressure and thruster firings may have lower noise than the accelerometer, and, depending on orbital altitude, atmospheric drag may be smaller than accelerometer noise.

The total instrument noise power spectral density is

$$S_a = S_{\text{ACC}} + S_{\text{LRI}}. \quad (17)$$

Figure 5 shows $\sqrt{S_a}$ for various instrument noise spectra.

As in section 2, define the signal-to-noise density for range acceleration

$$W'_a(f) = \frac{|a_R(f)|^2/M^2}{S_a(f)}. \quad (18)$$

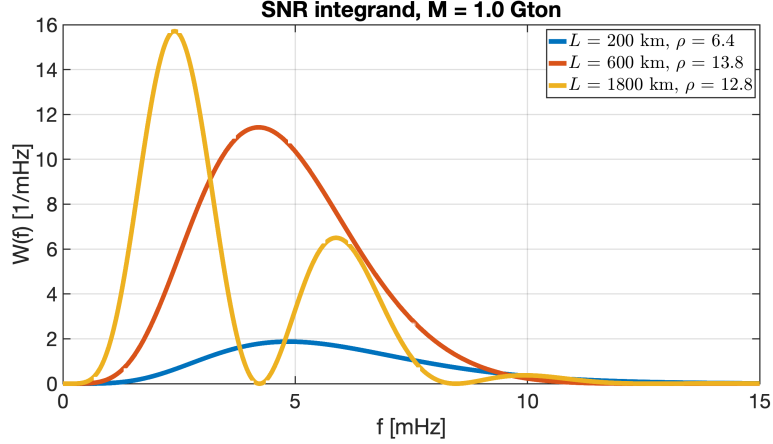


Figure 4. Signal-to-noise ratio integrand of Equation 18, $W_a(f)$ for the “GRAE-FO LRI + ACC” noise of Figure 5, signal from orbital altitude $h = 500$ km and source mass $M = 1$ Gton and several values of spacecraft separation L . The integrated signal-to-noise ratios ρ are indicated in the legend.

$W_a(f) = W'_a M^2$ is shown in Figure 4 for several values of L . The oscillations with nulls at multiples of $1/\tau = v_o/L$ degrade ρ for L beyond an optimum spacecraft separation.

The optimal signal to noise ratio per unit mass is

$$\rho' = \sqrt{4 \int_0^\infty W'_a(f) df}, \quad (19)$$

and the source mass that gives $\rho = 3$ is

$$M_3 = \frac{3}{\sqrt{4 \int_0^\infty W'_a(f) df}}. \quad (20)$$

From Equations 12 through 18 and Equation 20, the GRACE-FO parameters with the MWI and LRI give respectively $M_3 = 1.33$ Gton, 470 Mton. The corresponding detectable peak accelerations, $\kappa_R(L, h) \cdot M_3$, are 0.13 nm/s², 0.047 nm/s². In comparison, Ghobadi-Far et al. (2018) and Ghobadi-Far et al. (2020) analyze the line-of-sight gravity difference and find the estimation errors for the MWI and LRI to be 0.15 nm/s² and 0.10 nm/s², respectively. Considering that ibid used one year of data vs. our single-pass analysis, their resolvable acceleration estimates are considerably larger (and likely more realistic) than the ideal case analyzed here. See Section 3.4 for a comparison of the two very different filters that process range acceleration measurements. Another assessment of mass sensitivity for SST laser ranging is inferred from Colombo and Chao (1992), who proposed a laser ranging mission that, with $(h, L) = (600, 500)$ km was found by simulation to have sensitivity to weekly changes of 1 mm water height over a region 400 km across, or mass sensitivity of 160 Mton.

Figure 6 shows the mass sensitivity M_3 as a function of h and L for the LRI ranging instrument with two levels of accelerometer sensitivity: $\tilde{a}_0 = 1 \times 10^{-10}$ and 1×10^{-12} m/s²/√Hz. The optimum L for a given h depends weakly on the accelerometer noise, and is given approximately by $1.78h$ and $1.70h$ respectively. The lower row of Figure 6 shows the computed optimum L in comparison with these approximations, and the corresponding optimum M_3 .

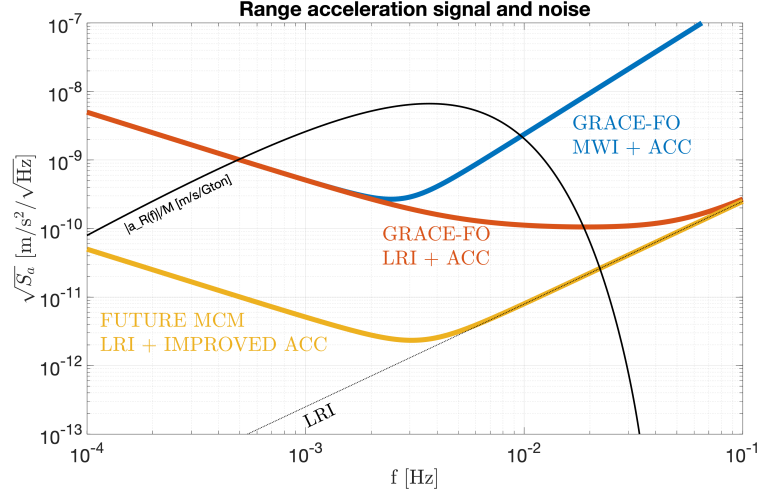


Figure 5. Total range acceleration noise rpsd $\sqrt{S_a}$ for various assumptions of instrument noise. The ranging noise for the “GRACE-FO MWI+ACC” is the white displacement noise of the microwave measurement on GRACE-FO, equal to $6 \times 10^{-7} \text{ m}/\sqrt{\text{Hz}}$. The other two noise curves assume the ranging noise of the LRI, Equation 14, shown as a dotted line. Two levels of $\bar{a}_0/[\text{m}/\text{s}^2/\sqrt{\text{Hz}}]$ are assumed: 1×10^{-10} for the GRACE-FO curves, and 1×10^{-12} for a future mission. The solid black line is the signal spectrum $a_R(f)$ from a 1 Gton point mass, for orbital altitude $h = 500 \text{ km}$ and separation $L = 200 \text{ km}$. The values of M_3 for the three respective configurations are 1.33 Gton, 470 Mton, 9.5 Mton.

3.4 Comparison to Line-of-sight Gravity Difference

The filter that gives maximum signal-to-noise ratio is (Wainstein and Zubakov (1970), Chapter 3)

$$G(f) = \frac{a_R^*(f)}{S_a(f)}, \quad (21)$$

with * denoting complex conjugation. The filter’s input is the measured range acceleration. $G(f)$ is an example of a filter for extracting a signal of known waveform, in this case the range acceleration resulting from flying over a point mass. Dropping the multiplicative constants, the filter magnitude is

$$|G(f)| = \frac{\left| f K_0 \left(\frac{2\pi f}{f_h} \right) \sin \left(\frac{2\pi f}{f_L} \right) \right|}{S_a(f)}. \quad (22)$$

$|G(f)|$ for the LRI on GRACE-FO is shown as the red trace in Figure 7.

Ghobadi-Far et al. (2018) define the gravimetric quantity $\delta g_{12}^{\text{LOS}}$, or line-of-sight gravity difference, which differs from the range acceleration residual $\ddot{\rho}$ by Δ_0 , the residual centrifugal acceleration:

$$\delta g_{12}^{\text{LOS}} = \delta \ddot{\rho} + \Delta_0. \quad (23)$$

Residuals are relative to a reference field. Admittance $Z(f)$ is defined as the transfer function

$$Z(f) = \frac{S_{a, \delta g_{12}^{\text{LOS}}}(f)}{S_a(f)} \quad (24)$$

where the numerator $S_{a, \delta g_{12}^{\text{LOS}}}(f)$ is the cross-power spectrum between of the range acceleration and the line-of-sight gravity difference (LGD). The denominator is written as $S_{\delta \ddot{\rho}, \delta \ddot{\rho}}$ in *ibid*.

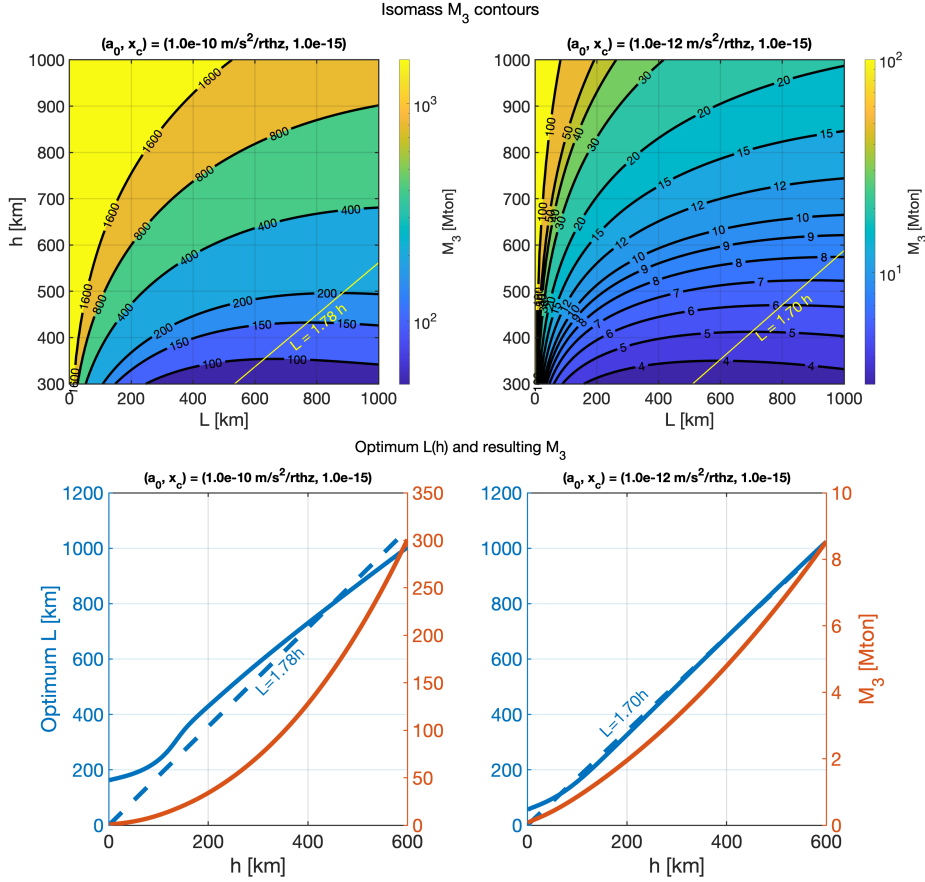


Figure 6. Mass sensitivity of of the LRI measurement on GRACE-FO *left*, and of a future GRACE-like mission *right*. Upper row shows isomass M_3 contours, in Mton, from Equation 5. Equation 14 specifies the ranging noise, and accelerometer noise is given by Equation 16 with $\tilde{a}_0 = (1 \times 10^{-10} \text{ m/s}^2/\sqrt{\text{Hz}}, 1 \times 10^{-12} \text{ m/s}^2/\sqrt{\text{Hz}})$ for the respective missions, with fixed $f_k = 5 \text{ mHz}$. The optimum satellite separation L as a function of orbital altitude h is given approximately by $L = (1.78, 1.70)h$, respectively. Lower row shows the precise optimum L as a function of h , (solid blue, left axis) and the resulting sensitivity M_3 (red, right axis).

$Z(f)$ normalized to have maximum value of 1 is shown as the blue trace in Figure 7. The passband for $Z(f)$ is 0.3 mHz to 20 mHz. Since $G(f)$ applies to a point mass, the field with the highest possible frequency content, its passband starts higher in frequency and spans 1 mHz to 20 mHz. A practical use for the $G(f)$ filter is searching for unknown point-like features, such as underground water storage of 100 km spatial extent. The filter would be applied to range acceleration measurements after subtracting the effect of the known field, including time-varying gravity, and non-gravitational accelerations.

Alternatively to the formulation in Section 3, the field from a point-like mass can be specified using the conventional spherical harmonic expansion for the gravitational anomaly. As shown in Appendix A, a perturbing mass of small spatial extent requires a large harmonic order to approximate its field.

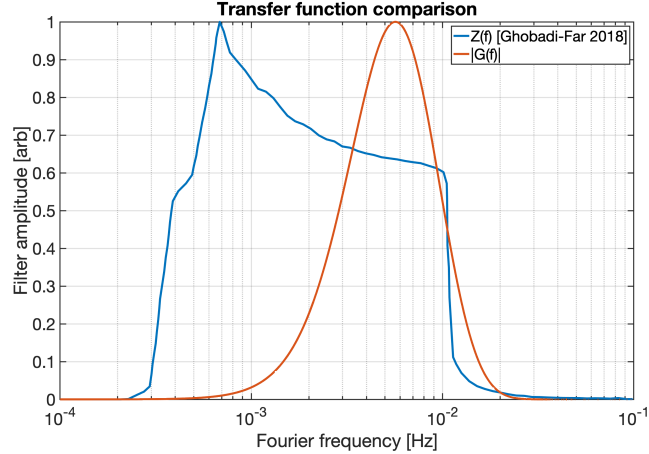


Figure 7. Two transfer functions for range acceleration data. $Z(f)$ is from Ghobadi-Far et al. (2018) Figure 2(b), and $G(f)$ is from Equation 21. Both transfer functions are normalized to give maximum value of 1.

4 Conclusion

The frequency response of an orbiting gradiometer to a point mass under the flight track is well-approximated by a simple equation (2) that depends only on the orbital altitude and the magnitude of the point mass. Likewise, for an SST-based measurement of the gravitational field the range acceleration has a simple expression (12) with additional dependency on the average satellite separation. Applying Wiener optimal filter theory, these responses and the noise spectra of the ranging measurement and of accelerometer-based measurement of non-gravitational forces give ρ , the maximum achievable signal-to-noise ratio. The resolvable mass M_3 is defined as the magnitude of the point mass that gives $\rho = 3$. M_3 is the ultimate mass sensitivity, and realistic non-point mass distributions that are not directly under the flight track will give larger M_3 in practice. Nonetheless, M_3 provides a figure of merit for comparing missions with different orbits and instrument sensitivities, serving as a guide the design of future missions. Additionally, for SST measurements M_3 has a minimum value at a specific satellite separation L , giving the optimum separation for discovering point-like (meaning less than approximately 300 km) features such as subsurface water storage. Equation 22 specifies the optimal filter for such a search.

Acknowledgments

The author thanks Kirk McKenzie, Gabriel Ramirez, Pep Sanjuan and David Wiese for useful discussions, and Christopher McCullough for key insights. This research was carried out at the Jet Propulsion Laboratory, California Institute of Technology, under a contract with the National Aeronautics and Space Administration. ©2020 California Institute of Technology. Government sponsorship acknowledged.

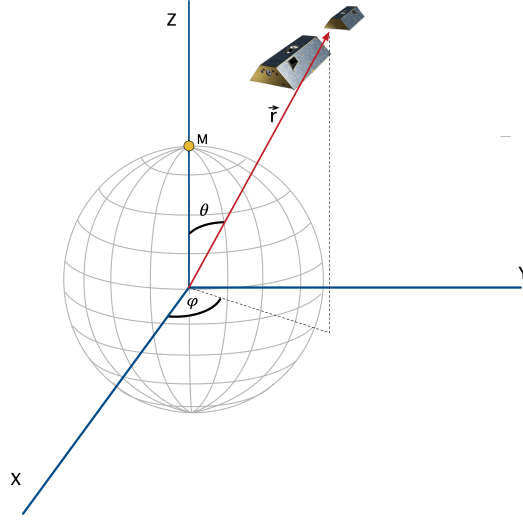


Figure A1. Coordinate system for the spherical harmonic expansion of geopotential, (Kaula, 2013). The satellite constellation position, defined as the center of mass for a gradiometer or (illustrated) the center of the line of sight between two SST satellites relative to the center of the Earth, is $\vec{r}(r, \theta, \phi)$, where r is the distance from the center of the Earth, θ is the co-latitude, and ϕ is the longitude.

Appendix A Multipole expansion and the Wahr equation for surface density

The gravitational potential is conventionally expressed as the multipole expansion (Kaula (1966), Kaula (2013), Chao and Gross (1987))

$$U(r, \theta, \phi) = \frac{GM_e}{a} \sum_{n=0}^{\infty} \sum_{m=0}^n \left(\frac{a}{r}\right)^{n+1} \bar{P}_{nm}(\cos \theta) (\bar{C}_{nm} \cos m\phi + \bar{S}_{nm} \sin m\phi). \quad (\text{A1})$$

As illustrated in Figure A1 $(r, \theta, \phi) =$ (distance from the center of the earth, co-latitude, longitude), $(a, M_e) =$ (Earth radius, Earth mass), and \bar{P}_{nm} is the fully-normalized associated Legendre function. The field is entirely specified by the Stokes coefficients $(\bar{C}_{nm}, \bar{S}_{nm})$.

For a known mass distribution $dM = \rho(r', \theta', \phi') dV'$, $(\bar{C}_{nm}, \bar{S}_{nm})$ are evaluated as the volume integral (Bettadpur, 2018)

$$\begin{bmatrix} \bar{C}_{nm} \\ \bar{S}_{nm} \end{bmatrix} = \frac{1}{(2n+1)M_e} \int_{V'} dM \left(\frac{r'}{a}\right)^n \bar{P}_{nm}(\mu') \begin{bmatrix} \cos m\phi' \\ \sin m\phi' \end{bmatrix}, \quad (\text{A2})$$

where $\mu' = \cos \theta'$. Equation A2 reduces for a point mass at $r' = a$ to

$$\begin{bmatrix} \bar{C}_{nm} \\ \bar{S}_{nm} \end{bmatrix} = \frac{M}{(2n+1)M_e} \bar{P}_{nm}(\mu') \begin{bmatrix} \cos m\phi' \\ \sin m\phi' \end{bmatrix}. \quad (\text{A3})$$

A single point mass can be placed at the north pole, $(\mu', \phi') = (0, 0)$ without loss of generality. There Equation A3 further reduces to

$$\begin{bmatrix} \bar{C}_{nm} \\ \bar{S}_{nm} \end{bmatrix} = \frac{M}{(2n+1)M_e} \bar{P}_{nm}(1) \begin{bmatrix} 1 \\ 0 \end{bmatrix}. \quad (\text{A4})$$

The relationship between fully normalized Legendre function \bar{P} and the associated Legendre function P is

$$\bar{P}_{nm} = \sqrt{\frac{(2 - \delta_{m0})(2n + 1)(n - m)!}{(n + m)!}} P_{nm}. \quad (\text{A5})$$

Using $P_{nm}(1) = \delta_{m0}$,

$$\bar{P}_{nm}(1) = \delta_{m0} \sqrt{2n + 1}, \quad (\text{A6})$$

and for a point mass at the pole Equation A4 finally reduces to

$$\begin{bmatrix} \bar{C}_{nm} \\ \bar{S}_{nm} \end{bmatrix} = \frac{M}{M_e} \frac{1}{\sqrt{2n + 1}} \begin{bmatrix} \delta_{m0} \\ 0 \end{bmatrix}. \quad (\text{A7})$$

The potential from Equations A1 and A7 is independent of ϕ and is given by the multipole expansion

$$U(r, \theta) = \frac{GM}{a} \sum_{n=0}^{\infty} \left(\frac{a}{r}\right)^{n+1} P_n(\cos \theta), \quad (\text{A8})$$

the familiar result from electrostatics for the azimuthally symmetric electric field from a point charge (Jackson, 2007).

The Wahr equation for surface density from $(\bar{C}_{nm}, \bar{S}_{nm})$ (Wahr et al., 1998) is

$$\sigma(\theta', \phi') = \frac{\alpha \rho_{\text{ave}}}{3} \sum_{n=0}^{\infty} \sum_{m=0}^n \bar{P}_{nm}(\cos \theta') \frac{2n + 1}{1 + k_n} (\bar{C}_{nm} \cos m\phi' + \bar{S}_{nm} \sin m\phi'), \quad (\text{A9})$$

where $k_n = \text{Love number}$. The surface density in the limit of small area can be compared to the point mass solution.

We use $(\bar{C}_{nm}, \bar{S}_{nm})$ for a spherical cap in the limit of small cap size to study the error of a finite-degree spherical harmonic approximation to a point mass. Consider a spherical cap centered at source coordinates (θ', ϕ') . The cap's angular radius is α and $\lambda \equiv \cos \alpha$. As computed by Pollack (1973), the Stokes coefficients are

$$\begin{bmatrix} \bar{C}_{nm} \\ \bar{S}_{nm} \end{bmatrix} = -\frac{M}{M_e} \frac{P_{n+1}(\lambda) - P_{n-1}(\lambda)}{(2n + 1)^2(1 - \lambda)} \bar{P}_{nm}(\lambda) \begin{bmatrix} \cos m\phi' \\ \sin m\phi' \end{bmatrix}. \quad (\text{A10})$$

For a spherical cap at the north pole,

$$\begin{bmatrix} \bar{C}_{nm} \\ \bar{S}_{nm} \end{bmatrix} = -\frac{M}{M_e} \frac{P_{n+1}(\lambda) - P_{n-1}(\lambda)}{(2n + 1)^{3/2}(1 - \lambda)} \begin{bmatrix} \delta_{m0} \\ 0 \end{bmatrix}. \quad (\text{A11})$$

The spherical cap reduces to a point mass in the limit of $\cos \alpha = 0$, or $\lambda = 1$. Substituting the limit

$$\lim_{\lambda \rightarrow 1} [P_{n+1}(\lambda) - P_{n-1}(\lambda)] = -(1 - \lambda)(2n + 1). \quad (\text{A12})$$

into Equation A11 gives Equation A7, as required for consistency.

By comparing expressions similar to Equation A1 and Equation A9, Dickey et al. (1997) identifies

$$\hat{C}_{nm} + \hat{S}_{nm} = \frac{\rho_{\text{ave}}}{3\rho_w} \frac{2n + 1}{1 + k_n} (\bar{C}_{nm} + \bar{S}_{nm}) \quad (\text{A13})$$

as the transformation to convert geoid expansion coefficients $(\bar{C}_{nm}, \bar{S}_{nm})$ to mass expansion coefficients $(\hat{C}_{nm}, \hat{S}_{nm})$, *ibid* p. 101 their Equation (B5).

At the pole $(\theta', \phi') = (0, 0)$ and $\lambda = 1$. From Equations A9 and A11, dropping the $n = 0$ term that represents the total potential of the Earth, and neglecting the

earth's elasticity by setting $k_n = 0$,

$$\sigma = \frac{a\rho_{\text{ave}}}{3} \sum_{n=1}^{\infty} \bar{P}_{nm}(1)(2n+1)\bar{C}_{nm} \quad (\text{A14})$$

$$= -\frac{M}{M_e} \frac{a}{1-\lambda} \frac{a\rho_{\text{ave}}}{3} \sum_{n=1}^{\infty} \bar{P}_{nm}^2(1) \frac{2n+1}{(2n+1)^2} (P_{n+1}(\lambda) - P_{n-1}(\lambda)) \quad (\text{A15})$$

$$= -\frac{M}{M_e} \frac{a}{1-\lambda} \frac{a\rho_{\text{ave}}}{3} \sum_{n=1}^{\infty} P_{n+1}(\lambda) - P_{n-1}(\lambda) \quad (\text{A16})$$

$$= \frac{M}{M_e} \frac{a\rho_{\text{ave}}}{3} T_{\infty}. \quad (\text{A17})$$

The quantity T_{∞} is the $N = \infty$ limit of the truncated sum, defined as

$$T_N(\lambda) = \frac{1}{1-\lambda} \sum_{n=1}^N P_{n-1}(\lambda) - P_{n+1}(\lambda) \quad (\text{A18})$$

$$= \frac{1}{1-\lambda} (P_0(\lambda) + P_1(\lambda) - (P_N(\lambda) + P_{N+1}(\lambda))) \quad (\text{A19})$$

$$= \frac{1+\lambda - (P_N(\lambda) + P_{N+1}(\lambda))}{1-\lambda} \quad (\text{A20})$$

For a small spherical cap, $\alpha \ll 1$ (and $\lambda = \cos \alpha$ slightly < 1), the cap area is $A = \pi(a\alpha)^2$. Using $\sigma = M/A$ and $\rho_{\text{ave}} = 3M_e/(4\pi a^3)$, Equation A17 is equivalent to

$$\frac{\alpha^2 T_{\infty}(\cos \alpha)}{4} - 1 = 0. \quad (\text{A21})$$

Define the error from truncating the sum at N ,

$$\epsilon_N = \frac{\alpha^2 T_N(\cos \alpha)}{4} - 1. \quad (\text{A22})$$

Figure A2 shows ϵ_N for small spherical caps of two different sizes. This numerical calculation is consistent with Equation A21 in the limit of very large N . As can be seen, ϵ_N approaches zero slowly, equalling 0.06 for $\alpha = 0.02$, with $N = 1 \times 10^4$. The slow convergence suggests that the unfiltered spherical harmonic expansion is ill-suited to characterizing the field from a point-like source. The truncation error is often reduced in geodesic analyses by applying a spectral localizing filter (Panet et al. (2013), Appendix 2); see also Wahr et al. (1998), Swenson and Wahr (2002), Seo et al. (2005), and Werth et al. (2009).

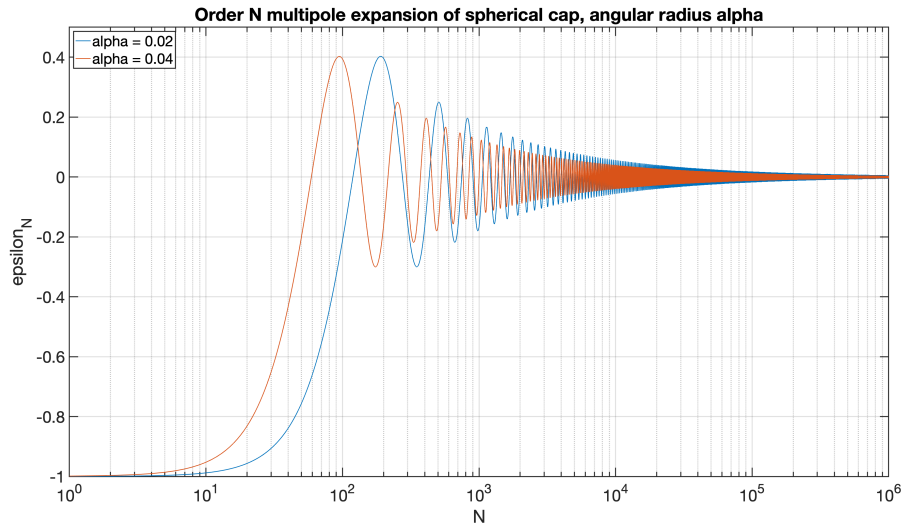


Figure A2. Truncation error, Equation A22, in representing the field from a mass of small spatial extent by spherical harmonic expansion of order N .

References

- Abich, K., Abramovici, A., Amparan, B., Baatzsch, A., Okihiro, B. B., Barr, D. C., ... others (2019). In-orbit performance of the GRACE Follow-on laser ranging interferometer. *Physical review letters*, *123*(3), 031101.
- Abramowitz, M., & Stegun, I. A. (1964). *Handbook of mathematical functions with formulas, graphs, and mathematical tables* (ninth Dover printing, tenth GPO printing ed.). New York: Dover.
- Bettadpur, S. (2018). GRACE L-2 product user manual [Computer software manual]. (GRACE 327-734, CSR-GR-03-01)
- Chao, B. F., & Gross, R. S. (1987). Changes in the earth's rotation and low-degree gravitational field induced by earthquakes. *Geophysical Journal International*, *91*(3), 569–596.
- Christophe, B., Marque, J., & Foulon, B. (2010). In-orbit data verification of the accelerometers of the ESA GOCE mission. In *Sf2a-2010: Proceedings of the annual meeting of the french society of astronomy and astrophysics* (Vol. 1, p. 113).
- Colombo, O., & Chao, B. (1992). Global gravitational change from space in 2001. In *Iag symposium, potsdam* (Vol. 112).
- Conklin, J., & Nguyen, A. N. (2017). Drag-free control and drag force recovery of small satellites. In *31st annual AIAA/USU conference on small satellites*.
- Dickey, J., Bentley, C. R., Bilham, R., Carton, J., Eanes, R., Herring, T. A., ... others (1997). Satellite gravity and the geosphere. *National Research Council Report*, 112.
- Drinkwater, M. R., Haagmans, R., Muzi, D., Popescu, A., Floberghagen, R., Kern, M., & Fehringer, M. (2006). The GOCE gravity mission: ESAs first core earth explorer. In *Proceedings of the 3rd international GOCE user workshop* (pp. 6–8).
- Flanagan, E. E., & Hughes, S. A. (1998, Apr). Measuring gravitational waves from binary black hole coalescences. i. signal to noise for inspiral, merger, and ringdown. *Phys. Rev. D*, *57*, 4535–4565. doi: 10.1103/PhysRevD.57.4535
- Ghobadi-Far, K., Han, S.-C., McCullough, C. M., Wiese, D. N., Yuan, D.-N., Landerer, F. W., ... Watkins, M. M. (2020). Grace follow-on laser ranging interferometer measurements uniquely distinguish short-wavelength gravitational perturbations. *Geophysical Research Letters*, *47*(16), e2020GL089445. Retrieved from <https://agupubs.onlinelibrary.wiley.com/doi/abs/10.1029/2020GL089445> (e2020GL089445 2020GL089445) doi: 10.1029/2020GL089445
- Ghobadi-Far, K., Han, S.-C., Weller, S., Loomis, B. D., Luthcke, S. B., Mayer-Gürr, T., & Behzadpour, S. (2018). A transfer function between line-of-sight gravity difference and GRACE intersatellite ranging data and an application to hydrological surface mass variation. *Journal of Geophysical Research: Solid Earth*, *123*(10), 9186–9201.
- Han, S.-C. (2013). Determination and localized analysis of intersatellite line of sight gravity difference: Results from the GRAIL primary mission. *Journal of Geophysical Research: Planets*, *118*(11), 2323–2337.
- Jackson, J. D. (2007). *Classical electrodynamics*. John Wiley & Sons.
- Kaula, W. M. (1966). Tests and combination of satellite determinations of the gravity field with gravimetry. *Journal of Geophysical Research*, *71*(22), 5303–5314.
- Kaula, W. M. (2013). *Theory of satellite geodesy: applications of satellites to geodesy*. Courier Corporation.
- Konopliv, A. S., Park, R. S., Yuan, D.-N., Asmar, S. W., Watkins, M. M., Williams, J. G., ... others (2013). The JPL lunar gravity field to spherical harmonic degree 660 from the GRAIL primary mission. *Journal of Geophysical Research: Planets*, *118*(7), 1415–1434.

- Landerer, F., Flechtner, F., Save, H., Webb, F., Bandikova, T., & Bertiger, e. a., WI. (2020). Extending the global mass change data record: GRACE followon instrument and science data performance. *Geophysical Research Letters*, *47*. doi: 10.1029/2020GL088306
- Numata, K., Kemery, A., & Camp, J. (2004). Thermal-noise limit in the frequency stabilization of lasers with rigid cavities. *Physical Review Letters*, *93*(25), 250602.
- Panet, I., Flury, J., Biancale, R., Gruber, T., Johannessen, J., van den Broeke, M., ... others (2013). Earth system mass transport mission (e. motion): a concept for future earth gravity field measurements from space. *Surveys in Geophysics*, *34*(2), 141–163.
- Pollack, H. N. (1973). Spherical harmonic representation of the gravitational potential of a point mass, a spherical cap, and a spherical rectangle. *Journal of Geophysical Research*, *78*(11), 1760–1768.
- Reigber, C., Schwintzer, P., Neumayer, K.-H., Barthelmes, F., König, R., Förste, C., ... others (2003). The champ-only earth gravity field model eigen-2. *Advances in Space Research*, *31*(8), 1883–1888.
- Seo, K.-W., Wilson, C., Chen, J., Famiglietti, J., & Rodell, M. (2005). Filters to estimate water storage variations from grace. In *A window on the future of geodesy* (pp. 607–611). Springer.
- Swenson, S., & Wahr, J. (2002). Methods for inferring regional surface-mass anomalies from gravity recovery and climate experiment (GRACE) measurements of time-variable gravity. *Journal of Geophysical Research: Solid Earth*, *107*(B9), ETG–3.
- Tapley, B. D., Bettadpur, S., Ries, J. C., Thompson, P. F., & Watkins, M. M. (2004). GRACE measurements of mass variability in the earth system. *Science*, *305*(5683), 503–505. doi: 10.1126/science.1099192
- Touboul, P., Willemenot, E., Foulon, B., & Josselin, V. (1999). Accelerometers for CHAMP, GRACE and GOCE space missions: synergy and evolution. *Bollettino di Geofisica Teorica ed Applicata*, *40*(3-4), 321–327.
- Wahr, J., Molenaar, M., & Bryan, F. (1998). Time variability of the earth’s gravity field: Hydrological and oceanic effects and their possible detection using GRACE. *Journal of Geophysical Research: Solid Earth*, *103*(B12), 30205–30229.
- Wainstein, L. A., & Zubakov, V. (1970). *Extraction of signals from noise*. Prentice-Hall, Englewood Cliffs, NJ.
- Watkins, M., Wiese, D. N., Yuan, D.-N., Boening, C., & Landerer, F. W. (2015). Improved methods for observing earth’s time variable mass distribution with grace using spherical cap mascons. *Journal of Geophysical Research: Solid Earth*, *120*(4), 2648–2671.
- Watkins, M., Yuan, D., Kuang, D., Bertiger, W., Kim, M., & Kruizinga, G. (2005). Grace harmonic and mascon solutions at jpl. *AGUFM, 2005*, G22A–04.
- Werth, S., Güntner, A., Schmidt, R., & Kusche, J. (2009). Evaluation of GRACE filter tools from a hydrological perspective. *Geophysical Journal International*, *179*(3), 1499–1515.
- Wolff, M. (1969). Direct measurements of the earth’s gravitational potential using a satellite pair. *Journal of Geophysical Research*, *74*(22), 5295–5300.
- Wong, L., Buechler, G., Downs, W., Sjogren, W., Muller, P., & Gottlieb, P. (1971). A surface-layer representation of the lunar gravitational field. *Journal of Geophysical Research*, *76*(26), 6220–6236.